ADVANCED FUNCTIONAL MATERIALS
www.afm-journal.de

Insights into Fullerene Passivation of SnO_2 Electron Transport Layers in Perovskite Solar Cells

*Junke Wang, Kunal Datta, Christ H. L. Weijtens, Martijn M. Wienk, and René A. J. Janssen**

Interfaces between the photoactive and charge transport layers are crucial for the performance of perovskite solar cells. Surface passivation of SnO_2 as electron transport layer (ETL) by fullerene derivatives is known to improve the performance of n–i–p devices, yet organic passivation layers are susceptible to removal during perovskite deposition. Understanding the nature of the passivation is important for further optimization of SnO_2 ETLs. X-ray photoelectron spectroscopy depth profiling is a convenient tool to monitor the fullerene concentration in passivation layers at a SnO_2 interface. Through a comparative study using [6,6]-phenyl-C_{61}-butyric acid methyl ester (PCBM) and [6,6]-phenyl-C_{61}-butyric acid (PCBA) passivation layers, a direct correlation is established between the formation of interfacial chemical bonds and the retention of passivating fullerene molecules at the SnO_2 interface that effectively reduces the number of defects and enhances electron mobility. Devices with only a PCBA-monolayer-passivated SnO_2 ETL exhibit significantly improved performance and reproducibility, achieving an efficiency of 18.8%. Investigating thick and solvent-resistant C_{60} and PCBM-dimer layers demonstrates that the charge transport in the ETL is only improved by chemisorption of the fullerene at the SnO_2 surface.

1. Introduction

Organic–inorganic hybrid perovskite solar cells (PSCs) have attracted unprecedented interests from the photovoltaic (PV) research community in recent years. Robust strategies have been developed for small-area devices with various perovskite compositions and device architectures, resulting in power conversion efficiencies (PCEs) well above 20%.[1–8] Compared to other PV technologies, perovskites present distinct advantages by combining high PCEs, with cost-effectiveness and solution processability, providing the incentive to explore large-area implementation.[9–12] In state-of-the-art n–i–p PSC architectures, mesoporous TiO_2 is commonly used as electron transport layer (ETL). Mesoporous TiO_2, however, requires a high temperature (≥450 °C) process, which limits its potential for upscalable processing on flexible substrates.[9,12,13] Numerous early studies[14–17] have pinpointed the excellent characteristics of lead halide perovskites, i.e., a high absorption coefficient, long carrier diffusion length and bipolar carrier transport, suggesting that high PCEs can also be achieved in planar PSCs, eliminating the mesoporous TiO_2 layer and the need for high temperature processing.

In the planar n–i–p PSC architecture, n-type semiconducting metal oxides with tailored compositions and structures have been extensively explored as the ETLs.[18,19] Tin oxide (SnO_2) is considered as a superior candidate for high-performing PSCs.[20–25] Compared to other metal oxides, it has been shown to provide better energy level alignment with the perovskite absorber, higher electron mobility, enhanced UV stability, and visible light transparency.[21,23,25,26] Recently, several low-temperature processing techniques such as the sol–gel layers,[21] atomic layer deposition,[25–27] and chemical bath deposition[28] have been utilized for high-quality planar SnO_2 ETLs. Moreover, by using a commercialized SnO_2 colloidal dispersion, the best PCE of SnO_2-based PSCs (23.32%) is now comparable to that of mesoporous-TiO_2 cells.[29] It is noteworthy, however, that metal oxides are prone to contain imperfections. Depending on the fabrication method, the number of defects (e.g., oxygen vacancies) of SnO_2 can vary dramatically, affecting device performance and stability.[22,30] Specifically, defects at the SnO_2/perovskite interface can induce ionic charge accumulation[31,32] and nonradiative interfacial recombination,[33] both contributing to the hysteresis effect and performance loss in PSCs.[31,34] Surface passivation of SnO_2 can considerably suppress the formation of interfacial defects.[20,33] By introducing an organic modification layer between the perovskite and SnO_2

J. Wang, K. Datta, Dr. C. H. L. Weijtens, Dr. M. M. Wienk, Prof. R. A. J. Janssen
Molecular Materials and Nanosystems
Institute of Complex Molecular Systems
Eindhoven University of Technology
P.O. Box 513, 5600 MB Eindhoven, The Netherlands
E-mail: r.a.j.janssen@tue.nl
Prof. R. A. J. Janssen
Dutch Institute for Fundamental Energy Research
De Zaale 20, 5612 AJ Eindhoven, The Netherlands
The ORCID identification number(s) for the author(s) of this article can be found under https://doi.org/10.1002/adfm.201905883.

© 2019 The Authors. Published by WILEY-VCH Verlag GmbH & Co. KGaA, Weinheim. This is an open access article under the terms of the Creative Commons Attribution-NonCommercial License, which permits use, distribution and reproduction in any medium, provided the original work is properly cited and is not used for commercial purposes.

DOI: 10.1002/adfm.201905883

16163028, 2019, 46, Downloaded from https://advanced.onlinelibrary.wiley.com/doi/10.1002/adfm.201905883 by Junke Wang - Oxford University , Wiley Online Library on [28/03/2026]. See the Terms and Conditions (https://onlinelibrary.wiley.com/terms-and-conditions) on Wiley Online Library for rules of use; OA articles are governed by the applicable Creative Commons License

layers, PSCs exhibit reduced interfacial loss, less pronounced hysteresis, and thereby better PV performance.[30,33,35–39]

There are some prerequisites for the efficient surface passivation of SnO_2.[19,40] First is the activation of the SnO_2 surface.[40] By UV–ozone treatment, organic binders and adventitious contaminants of SnO_2 can easily be removed while the number of surface-bound hydroxyl groups is increased, providing more anchoring sites for the passivation layer.[22,41,42] Second, a judicious selection of organic surface modifier is required. Fullerene derivatives, as well as other carboxylate self-assembled monolayers (SAMs), are among the most studied owing to the ease of forming covalent bonds between the carboxylate moiety and SnO_2 surface, and the broad availability of electron-accepting groups which passivate the SnO_2/perovskite interface.[19,33,35–39,43–46] Third, the deposition condition of organic modifiers could also affect their binding strength toward the substrate.[19] While no special treatment is required for carboxylic acid-based SAMs,[35,47–49] a thermal treatment is commonly used when employing passivation by [6,6]-phenyl-C_{61}-butyric acid methyl ester (PCBM)[37,38,48] to enhance binding to the SnO_2 surface. However, it is remarkable that most organic modifiers are not solvent-resistant and can easily be removed by spin coating of the perovskite precursors.[50–56] Despite improving the PCE,[35,39] very few studies were able to pinpoint the whereabouts of the passivation layer.[47,56–58] Therefore, the direct correlation between the presence of interfacial modifiers and the PSC performance remains obscure. On the other hand, tremendous research efforts have been made to improve the robustness of the organic modification layer, for instance, by introducing thermal evaporated C_{60}[37,48,59] or by developing cross-linkable fullerene derivatives,[53–55,60,61] after which a bilayered ETL in the device can be formed. In this case, however, the impact of a chemical interaction between the SnO_2 and passivation layer is often neglected.

Herein, we use three representative fullerenes, C_{60}, PCBM, and [6,6]-phenyl-C_{61}-butyric acid (PCBA) (**Figure 1**) to passivate a SnO_2 ETL in planar n–i–p PSCs. Through X-ray photoelectron spectroscopy (XPS) depth profiling we reveal the precise distribution of fullerenes in the ETL. It is found that a PCBA monolayer easily binds to the SnO_2 interface, whereas a PCBM monolayer can only be created and preserved when employing a thermal annealing treatment prior to depositing the perovskite. We demonstrate that fullerenes with the ability to react with surface hydroxyl groups effectively passivate defects at the SnO_2 interface and improve the performance and reproducibility of the PSCs. After optimization, the best-performing device with a PCE of 18.8% is achieved by using PCBA-monolayer-passivated SnO_2. Although thermally evaporated C_{60} is mostly retained after the solvent treatment, the deteriorated PV performance indicates that no efficient passivation is developed at the SnO_2 interface. By exposing an as-deposited PCBM layer to UV light, a less-soluble dimeric state of PCBM is obtained,[62–64] which enabled us to further study the role of fullerene passivation in a bilayered SnO_2/fullerene ETL configuration. It is found that even when the SnO_2 surface is fully covered by a PCBM-dimer layer, the charge transport in the ETL remains inefficient unless thermal annealing is applied after depositing PCBM. Our results highlight that chemisorption (PCBA) rather than physisorption (C_{60} and PCBM) to SnO_2 is the most influential factor in enhancing the interfacial charge transport process.

2. Results and Discussion

Planar n–i–p PSCs were fabricated based on an indium tin oxide (ITO)/SnO_2/perovskite/Spiro-OMeTAD/MoO_3/Au device structure, in which the SnO_2 ETL is spin coated from a colloidal dispersion and passivated by different fullerene layers. A double-cation perovskite $FA_{0.66}MA_{0.34}PbI_{2.85}Br_{0.15}$ (FA is formamidinium, and MA is methylammonium) was deposited on the ETL via a facile two-step solution process reported by Qiu et al.[55,65] To optimize processing conditions for the ETL, we started using a SnO_2 layer (≈20 nm), spin coated from an ≈2.8 wt% colloidal aqueous solution,[23] thermally annealed in air at 150 °C, and treated by UV–ozone before depositing PCBM from chlorobenzene (10 mg mL^{-1}) and subsequent annealing at 100 °C for 20 min. The UV–ozone treatment increases the open-circuit voltage (V_{oc}) from 0.97 to 1.04 V (Figure S1 and Table S1, Supporting Information). XPS confirmed that together with the removal of carbon contaminant or organic binders of the SnO_2 layer,[42] a more hydroxylated SnO_2 surface is obtained after UV–ozone treatment, which promotes the passivation of SnO_2 by PCBM (Figure S2 and Table S2, Supporting Information).[66] Different from a previous study,[23] we found that the V_{oc} of PSCs can be further improved when increasing the thickness of the SnO_2 layer from ≈20 to ≈110 nm (Figure S3 and Table S3, Supporting Information) because of better coverage and reduced shunting pathways.[67] Surprisingly, the fill factor (FF) is not influenced when increasing the SnO_2 layer thickness, owing to its high electron mobility (Table S3, Supporting information). As a result, optimum PSC performance was achieved by using 10 min. UV–ozone treated ≈110 nm SnO_2 layers as ETL.

To study the effect of fullerene passivation on the device performance, C_{60}, PCBM, and PCBA were introduced at the SnO_2/perovskite interface, either with or without a thermal annealing treatment at 100 °C for 20 min. in N_2 atmosphere. **Figure 2** and Figure S4 in the Supporting Information show the statistical distribution of performance characteristics (short-circuit current density J_{sc}, V_{oc}, FF, and PCE) of the devices with different passivation layers. The corresponding averaged PV parameters are summarized in Table S4 (Supporting Information) for the

Figure 1. Chemical structure of C_{60}, PCBM, and PCBA.

© 2019 The Authors. Published by WILEY-VCH Verlag GmbH & Co. KGaA, Weinheim

16163028, 2019, 46, Downloaded from https://advanced.onlinelibrary.wiley.com/doi/10.1002/adfm.201905883 by Junke Wang - Oxford University , Wiley Online Library on [28/03/2026]. See the Terms and Conditions (https://onlinelibrary.wiley.com/terms-and-conditions) on Wiley Online Library for rules of use; OA articles are governed by the applicable Creative Commons License

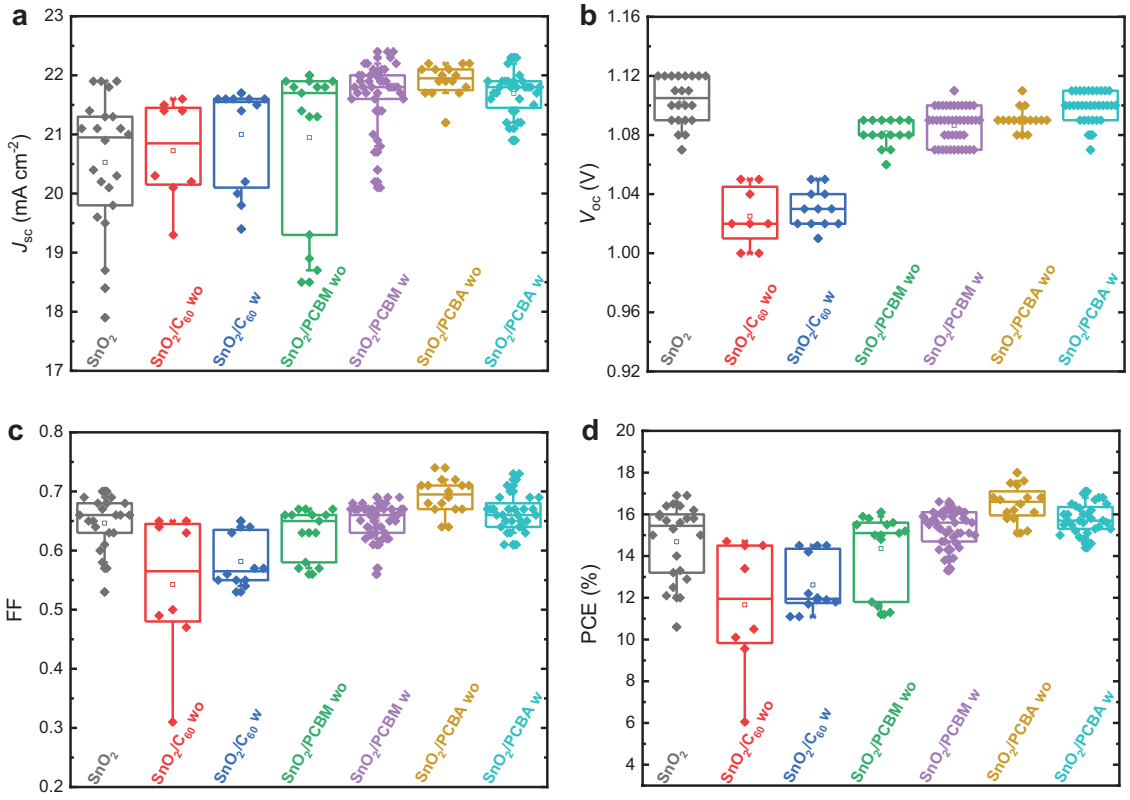

Figure 2. Statistical distribution of a) J_{sc}, b) V_{oc}, c) FF, and d) PCE of the ITO/SnO_2/fullerene/$FA_{0.66}MA_{0.34}PbI_{2.85}Br_{0.15}$/Spiro-OMeTAD/$MoO_3$/Au PSCs using different fullerene passivation layers, with (w) or without (wo) thermal annealing, and measured in a reverse scan.

reverse scan (from V_{oc} to J_{sc}) and forward scan (from J_{sc} to V_{oc}). Figure 2 demonstrates that without a passivation layer the SnO_2 control device exhibits a significant spread in performance, showing an average PCE of 14.7 ± 1.79% in the reverse scan and 13.0 ± 2.45% in the forward scan. The significant differences can be ascribed to an uncontrolled number of trap states, which induces localized ionic charges at the SnO_2/perovskite interface and results in the formation of a potential barrier that hampers the charge extraction process.[31]

To test the effect of interfacial passivation layers, we first employed a thermally evaporated C_{60} layer. It has previously been reported that ≥35 nm thick C_{60} layers are needed to retain complete coverage of the substrate after processing the perovskite layer from solution without changing its electron transport properties.[59] However, we find that devices with a thermally evaporated C_{60} layer (35 nm) performed inferior compared to the SnO_2 device. The V_{oc} is reduced from 1.10 ± 0.02 to 1.03 ± 0.02 V, while the FF drops from 0.65 ± 0.04 to 0.54 ± 0.12, resulting in a moderate PCE of 11.7 ± 3.12% (in the reverse scan). The low FF is ascribed to a high series resistance, resulting from the thick C_{60} layer. Thermal annealing of the C_{60} layer provides only a marginal improvement, delivering an average PCE of 12.6 ± 1.38% (in the reverse scan). To reduce the effect of a high series resistance, PSCs with thinner C_{60} interfacial layers were tested but their performance remained inferior to the SnO_2 device without passivation (Figure S5, Supporting Information). These results demonstrate that inserting a C_{60} layer at the SnO_2/perovskite interface affords no effective passivation, but rather restricts the electron extraction and induces nonradiative interfacial recombination, lowering both the FF and V_{oc}.

In a second step, we used an ≈15 nm PCBM interfacial layer applied by solution processing from chlorobenzene (10 mg mL^{-1}). The PV characteristics are almost identical to the SnO_2 device without a passivation layer. A similar broad distribution of PCEs is observed for both the reverse scan (14.4 ± 1.84%) and the forward scan (14.1 ± 1.98%). However, thermal treatment of the PCBM layer (100 °C, 20 min. under N_2) prior to depositing the perovskite layer results in a significant enhancement in performance and reproducibility. Compared to the bare SnO_2 device, the annealed PCBM device displays a higher average PCE of 15.3% and a small standard deviation of 0.84% in the reverse scan, due to an increased J_{sc} of 21.7 ± 0.56 mA cm^{-2}, a comparable V_{oc} of 1.09 ± 0.01 V, and an FF of 0.65 ± 0.03. The PCE difference between both scanning directions is negligible, by showing an average PCE of 15.5 ± 0.86% in the forward scan. Apparently thermal annealing leads to a passivated ETL interface that remains intact during the perovskite solution processing. Possibly, thermal annealing causes the ester side chains of PCBM to react with the hydroxyl groups of the SnO_2 surface, forming covalent bonds.

In accordance with this idea, a PCBA monolayer[47] spin coated from a dilute (0.2 mg mL^{-1}) solution in dichlorobenzene, exhibits a distinctively improved passivation compared to PCBM or C_{60}, regardless of the thermal annealing process. Without thermal annealing PCBA gives the best performance, showing a PCE of 16.5 ± 0.84% in the reverse scan, with a reduced standard deviation

© 2019 The Authors. Published by WILEY-VCH Verlag GmbH & Co. KGaA, Weinheim

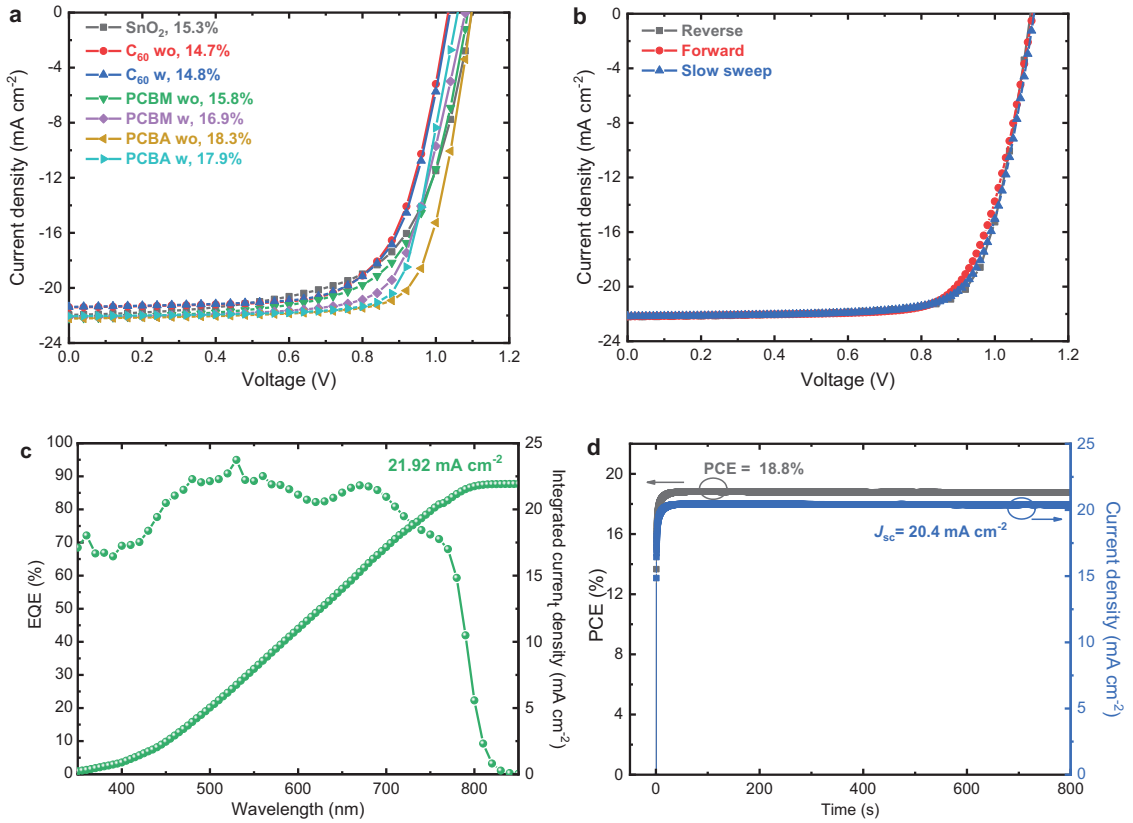

Figure 3. a) Stabilized *J–V* curves of the best-performing ITO/SnO_2/fullerene/$FA_{0.66}MA_{0.34}PbI_{2.85}Br_{0.15}$/Spiro-OMeTAD/$MoO_3$/Au solar cells with different passivation layers, with (w) or without (wo) thermal annealing. b) *J–V* curves and c) EQE spectra of the champion device with SnO_2/PCBA (not-annealed). d) Steady-state power and photocurrent output tracking over time of the champion device operated at the maximum power point under the 100 mW cm^{-2} simulated AM1.5G illumination condition.

in a J_{sc} of 21.9 ± 0.26 mA cm^{-2}, a V_{oc} of 1.09 ± 0.01 V, and a significantly improved FF of 0.69 ± 0.03. Comparable high performance is also obtained in the forward scan, with an average PCE of 16.9 ± 0.78%. This supports the idea that the higher reactivity of the carboxylic acid side chain in PCBA toward the hydroxyl groups of the SnO_2 surface play a role in the improved passivation.

We note that the PCEs reported here are lower than the record efficiencies,[29] but the clear trends in the statistical distributions of device performance support the effectiveness of the fullerene passivation at the SnO_2/perovskite interface. **Figure 3**a and Figure S6 in the Supporting Information display the stabilized current density–voltage (*J–V*) curves and external quantum efficiency (EQE) spectra of the champion (i.e., highest PCE) PSCs for the different passivation conditions. The corresponding parameters are summarized in **Table 1**. Similar to the distributions shown in Figure 2, the devices based on not-annealed PCBA, annealed PCBA, and annealed PCBM exhibit the best performance, with PCEs of 18.3%, 17.9%, and 16.9%, respectively. The enhanced performance of the PCBA modified devices is mainly a consequence of the improved FF of 0.76, which suggests an improved electron extraction, originating from an efficiently passivated SnO_2 ETL. The best-performing PSC device based on PCBA

Table 1. Photovoltaic parameters of the champion PSCs with different fullerene layers.

Passivation layer	J_{sc}[a)] [mA cm^{-2}]	V_{oc}[a)] [V]	FF[a)]	PCE[a)] [%]	J_{sc}[b)] [mA cm^{-2}]	PCE[c)] [%]
SnO_2 reference	22.0	1.10	0.64	15.4	21.7	15.3
C_{60} not-annealed	21.4	1.03	0.69	15.3	20.7	14.7
C_{60} annealed	21.4	1.04	0.69	15.3	20.9	14.8
PCBM not-annealed	22.2	1.09	0.67	16.1	21.6	15.8
PCBM annealed	22.1	1.08	0.72	17.1	21.7	16.9
PCBA not-annealed	22.2	1.10	0.76	18.6	21.9	18.3
PCBA annealed	22.1	1.06	0.77	18.0	22.0	17.9

[a)]The data were extracted from stabilized *J–V* curves under simulated AM1.5G illumination (100 mW cm^{-2}); [b)]Calculated by integrating the EQE spectrum with the AM1.5G spectrum; [c)]Corrected PCE obtained by calculating the J_{sc} integrated from EQE spectrum and V_{oc} and FF from the stabilized *J–V* measurement.

© 2019 The Authors. Published by WILEY-VCH Verlag GmbH & Co. KGaA, Weinheim

16163028, 2019, 46, Downloaded from https://advanced.onlinelibrary.wiley.com/doi/10.1002/adfm.201905883 by Junke Wang - Oxford University , Wiley Online Library on [28/03/2026]. See the Terms and Conditions (https://onlinelibrary.wiley.com/terms-and-conditions) on Wiley Online Library for rules of use; OA articles are governed by the applicable Creative Commons License

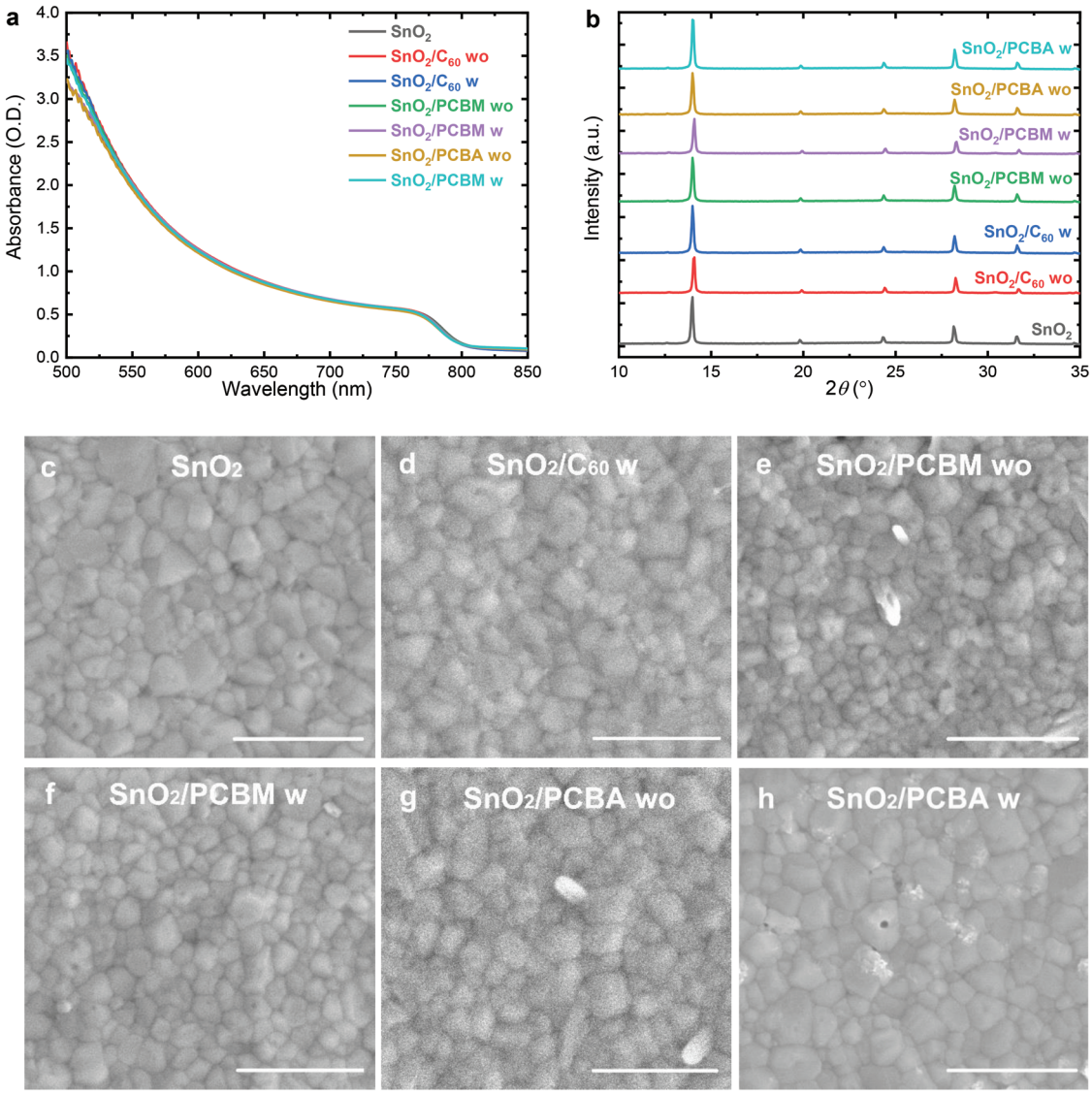

Figure 4. a) UV–vis–NIR spectra and b) XRD patterns of $FA_{0.66}MA_{0.34}PbI_{2.85}Br_{0.15}$ perovskite films deposited on different ETLs with (w) or without (wo) thermal annealing. Top-view SEM images of perovskite films on c) SnO_2, d) SnO_2/C_{60} (annealed), e) SnO_2/PCBM (not-annealed), f) SnO_2/PCBM (annealed), g) SnO_2/PCBA (not-annealed), and h) SnO_2/PCBA (annealed). Scale bars are 1 µm.

exhibits negligible hysteresis, by showing almost identical *J*–*V* curves (Figure 3b) measured in reverse, forward, and stabilized scans. The EQE measured with bias illumination provides an estimated J_{sc} in close correspondence with the *J*–*V* data measured with simulated AM1.5G (100 mW cm^{-2}) illumination (Figure 3c). Figure 3d shows the steady-state power and photocurrent output of the best device, measured at its maximum power point (V_{MPP} = 0.92 V) for 800 s. In this experiment the PCBA-modified device exhibits a photocurrent of 20.4 mA cm^{-2} and a PCE of 18.8%, which is very close to the values extracted from the *J*–*V* curves.

To validate our hypothesis that the device performance is determined by the electron transport properties of the ETL, we investigated the quality of the perovskite films deposited on different fullerene passivated SnO_2 substrates. All perovskite films display similar UV–vis–NIR absorption spectra, with a characteristic onset at around 800 nm (**Figure 4**a). Also, the X-ray diffraction (XRD) patterns of the as-prepared perovskite films are virtually identical (Figure 4b). No significant shift in the diffraction peak positions or intensities are observed, indicating that the crystallinity of perovskites is largely independent on the underlying fullerene layers. The primary diffraction peaks at 14° and 28° are assigned to the (110) and (220) lattice planes of the perovskite structure, respectively, and no significant trace of PbI_2 and nonperovskite phase can be identified. Figure 4c–h displays the top-view scanning electron microscope (SEM) images of the corresponding perovskite films deposited on different ETLs. All the layers exhibit a compact and pinhole-free surface morphology, with an average grain size of ≈300 nm. We attribute the independence of the perovskite morphology and crystallinity on different substrates to the two-step solution process utilized for depositing the perovskite layer, in which the crystallization dynamics are affected by the inorganic PbI_2

© 2019 The Authors. Published by WILEY-VCH Verlag GmbH & Co. KGaA, Weinheim

16163028, 2019, 46, Downloaded from https://advanced.onlinelibrary.wiley.com/doi/10.1002/adfm.201905883 by Junke Wang - Oxford University , Wiley Online Library on [28/03/2026]. See the Terms and Conditions (https://onlinelibrary.wiley.com/terms-and-conditions) on Wiley Online Library for rules of use; OA articles are governed by the applicable Creative Commons License

framework rather than the ETL substrate.[33,68] In addition, comparable results are obtained from the steady-state photoluminescence (PL) spectra and light-intensity dependent measurements (Figures S7 and S8, Supporting Information), showing that the bulk properties of perovskite layers remain unchanged on different ETLs. Accordingly, we rule out the impact of perovskite bulk properties on the variation trend of device performance.

To gain insight into the distribution of the fullerene in the passivation layers, we performed XPS depth profiling. We checked that the XPS depth profiles of pristine SnO_2 layers show no significant amounts of carbon (<1 at%) after UV–ozone cleaning (Figure S9, Supporting Information). Also, after subsequent rinsing with *N*,*N*-dimethylformamide (DMF) the carbon concentration remains negligible. Atomic force microscopy revealed that the root-mean-square average surface roughness of the nonpassivated and fullerene-passivated SnO_2 layers was less than 1 nm (Figure S10, Supporting Information). Hence, by monitoring the carbon signal of fullerene-passivated SnO_2 layers we can determine the fullerene concentration profile. **Figure 5**a,b shows the XPS depth profiles of SnO_2 substrates with annealed and not-annealed PCBM layers after rinsing with DMF. In both cases, the tin concentration increases abruptly from the surface (t = 0 s), suggesting that DMF has removed most of the capping PCBM layer. Meanwhile, the carbon concentration of the annealed PCBM substrate is remarkably higher (29 at%) than that of the not-annealed PCBM substrate (11 at%). From the attenuated Sn 3d signal (Figure 5e),[49] we estimate the thickness of the annealed and not-annealed PCBM layers at the SnO_2 interface to be 1.3 and 0.2 nm, respectively. This implies that without thermal annealing, the interfacial PCBM layer is almost entirely removed by DMF, and no passivation can be developed at the SnO_2 interface; however, with annealing a PCBM-monolayer-passivated SnO_2 interface is formed, which remains intact during the solution processing. Interestingly, both SnO_2/PCBM substrates exhibit a plateau of the carbon signal (>7 at%) during the sputtering process. This suggests that PCBM infiltrates into the porous SnO_2 layer and that DMF does not remove such penetrated PCBM. These SnO_2 layers have been shown to have pore sizes on the order of 10 nm.[42] On the other hand, for the annealed and not-annealed PCBA-modified SnO_2 substrates, after DMF rinsing, the carbon concentrations at the surface (t = 0 s) are 43 and 40 at% (Figure 5c,d), much higher than their PCBM counterpart. From Figure 5e, the thicknesses of the interfacial PCBA layers are estimated to be 1.9 nm (annealed) and 1.6 nm (not-annealed), respectively, indicating that a PCBA monolayer with better coverage is obtained at the SnO_2 interface. It is also found that when compared to the nonpassivated SnO_2, the shift in the binding energies of Sn 3d core level for both the PCBA modified SnO_2 (>0.14 eV) is higher than that for the annealed- and not-annealed-PCBM modified SnO_2 (0.10 and 0.03 eV), respectively. Here, the positive shift of the Sn 3d peaks is attributed to the decreased electron density near the Sn atoms, which could be induced by the bonding between the SnO_2 surface and the fullerenes.[39,69] The results confirms the higher reactivity of the carboxylic acid functional group of PCBA than the methyl ester side of PCBM toward the hydroxyl (−OH) enriched SnO_2 surface in forming stable monolayers. The corresponding high-resolution XPS spectra of the C 1s and O 1s signals are shown in Figure S11 in the Supporting Information. The depth profiles (Figure 5c,d) also show that PCBA penetrates less deep into the SnO_2 layer than PCBM, which we attribute to the use of a diluted PCBA solution (0.2 mg mL^{-1}) compared to the PCBM solution (10 mg mL^{-1}). The fact that PCBA penetrates less deep into the SnO_2 layer as compared to PCBM, while at the same time the PCBA concentration at the SnO_2 surface is higher, confirms that the carbon signals for the PCBM samples are unlikely due to ion knock-on effects. Together with the PV performance derived from the PCBA and PCBM modified ETLs, we conclude that only the fullerenes located at the SnO_2/perovskite interface are essential for the interfacial passivation process.

XPS depth profiles for the C_{60}-modified SnO_2 substrates after DMF rinsing (Figure S12, Supporting Information) show that the carbon concentration only starts to decrease after a long-sputtering process when the as-deposited C_{60} layer is above 15 nm. This indicates that the thermally evaporated C_{60} layer is resilient against DMF solvent treatment. However, for the 5 nm thick C_{60} layer, the carbon concentration at the surface (t = 0 s) is reduced to 18 at%, only slightly higher than that of the not-annealed PCBM substrate (11 at%). Compared to the device with not-annealed PCBM, the 5 nm thick C_{60} modified device exhibits decreased PV performance (Figure S5, Supporting Information).

To verify the observations from the XPS analysis, UV–vis–NIR absorption spectra were measured for different fullerene modified SnO_2 layers deposited on quartz substrates before and after DMF rinsing (Figure 5f). As expected, the SnO_2/C_{60} (15 nm) substrate only displays a slight decrease in absorbance due to the high resilience of the C_{60} film against DMF treatment. In contrast, a significant reduction in absorbance is observed for both SnO_2/PCBM substrates with (w) or without (wo) annealing, since DMF washes away most of the capping PCBM layer. However, it is found that the absorbance of the annealed PCBM is still higher than that of the not-annealed PCBM, which confirms that more PCBM is retained on the substrate when thermally annealed. For PCBA-modified SnO_2 substrates, the absorbance before DMF rinsing is already low due to the dilute (0.2 mg mL^{-1}) PCBA solution used. After DMF rinsing both the annealed and not-annealed PCBA substrates show a negligible reduction in absorbance, confirming that DMF rinsing removes very little PCBA. Among the DMF-washed PCBM and PCBA passivation layers, the annealed PCBM layer exhibits the highest absorbance. This is attributed to the PCBM infiltrated into the SnO_2 layer that cannot be removed by DMF, as is evidenced by the XPS depth profiles (Figure 5a,b).

To explore the impact of PCBM (annealed) and PCBA monolayers on the passivation of the SnO_2 ETL, their energy band structures were characterized by ultraviolet photoelectron spectroscopy (UPS). **Figure 6**a depicts that the secondary electron edge of the SnO_2 layer shifts to lower binding energies after PCBM and PCBA passivation. This corresponds to a significant increase in the work function from 3.58 eV for the pristine SnO_2, to 3.80 and 4.00 eV for the PCBM- and PCBA-passivated SnO_2, respectively. From the onset of the valence band spectrum, the ionization potential of the SnO_2, SnO_2/PCBM, and SnO_2/PCBA films are calculated to be 7.60, 6.11, and 6.28 eV, respectively. Figure 6b illustrates a schematic energy level diagram

© 2019 The Authors. Published by WILEY-VCH Verlag GmbH & Co. KGaA, Weinheim

16163028, 2019, 46, Downloaded from https://advanced.onlinelibrary.wiley.com/doi/10.1002/adfm.201905883 by Junke Wang - Oxford University , Wiley Online Library on [28/03/2026]. See the Terms and Conditions (https://onlinelibrary.wiley.com/terms-and-conditions) on Wiley Online Library for rules of use; OA articles are governed by the applicable Creative Commons License

16163028, 2019, 46, Downloaded from https://advanced.onlinelibrary.wiley.com/doi/10.1002/adfm.201905883 by Junke Wang - Oxford University , Wiley Online Library on [28/03/2026]. See the Terms and Conditions (https://onlinelibrary.wiley.com/terms-and-conditions) on Wiley Online Library for rules of use; OA articles are governed by the applicable Creative Commons License

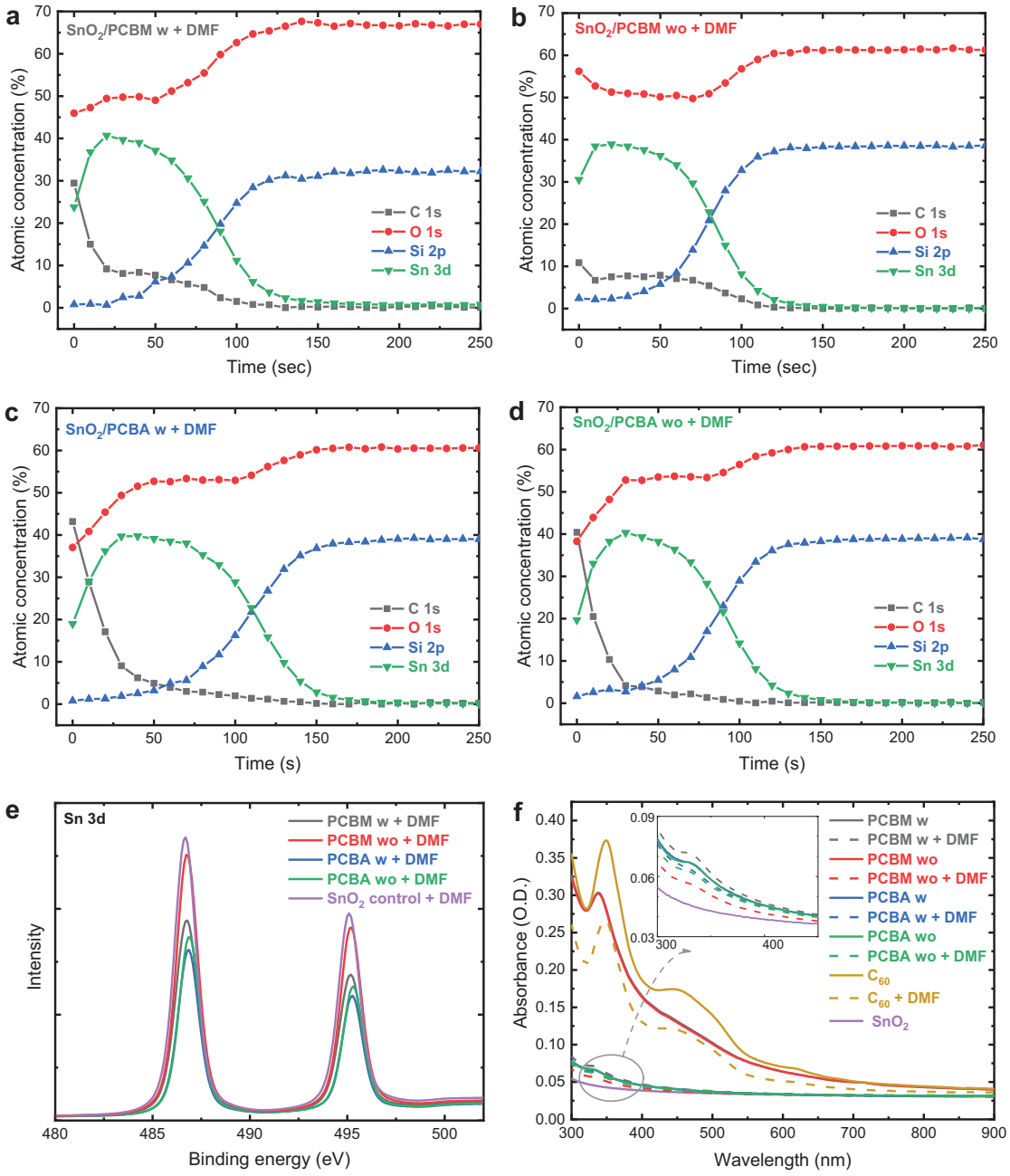

Figure 5. XPS depth profiles of a) SnO_2/PCBM (annealed), b) SnO_2/PCBM (not-annealed), c) SnO_2/PCBA (annealed), and d) SnO_2/PCBA (not-annealed) ETLs deposited on glass substrates. Layers were rinsed by DMF solvent shortly before the XPS experiments. e) XPS high-resolution scan spectra of the Sn 3d core level for different ETL substrate surfaces. f) UV–vis–NIR absorption spectra of different fullerene-passivated SnO_2 ETLs deposited on quartz substrates, measured before and after DMF rinsing. The initial SnO_2 layer thickness was ≈20 nm for all depth profiles.

for different ETLs, assuming a fixed Fermi level for all the measurements.[70] Consistent with the shift in Sn 3d binding energies (Figure 5e), the increase in work function of PCBM- and PCBA-passivated SnO_2 ETLs can be attributed to the formation of surface dipoles, which induce an electric field that accelerates the charge collection at the SnO_2 interface and reduces the recombination losses.[33,71] Figure 6c illustrates that compared to the pristine SnO_2, the PCBM- and PCBA-passivated SnO_2 ETLs exhibit better conduction band alignment with the perovskite, which could also be beneficial for the interfacial charge transport.

Based on the XPS analysis, one might expect that introduction of a better-covered PCBM layer at the SnO_2 interface would improve the device performance. Alternatively, an interfacial chemical reaction between the PCBM and SnO_2 could be of vital importance for improving the charge extraction. To gain further understanding of the role of PCBM interlayer, we introduced a solvent-resistant PCBM layer on the SnO_2. Following

© 2019 The Authors. Published by WILEY-VCH Verlag GmbH & Co. KGaA, Weinheim

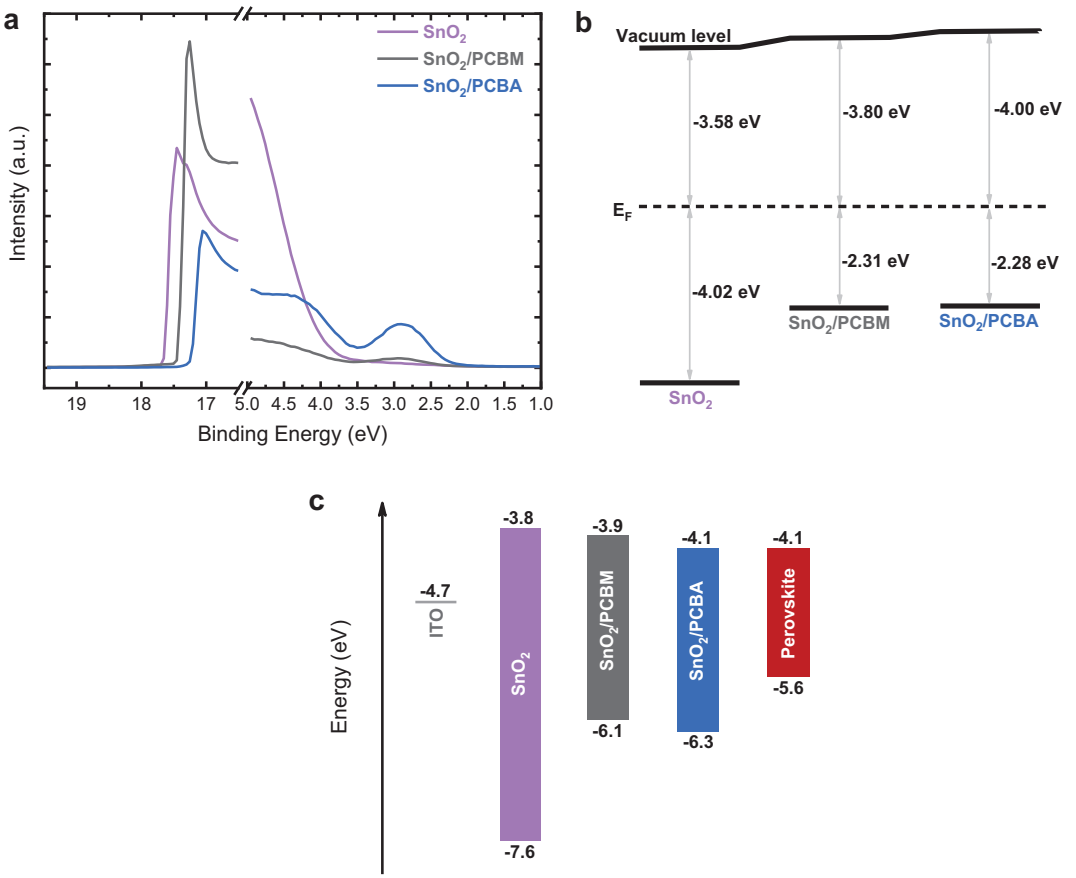

Figure 6. a) UPS measurements of SnO_2, SnO_2/PCBM, and SnO_2/PCBA, respectively. All samples were rinsed by DMF before the measurement. b) Energy diagram of different ETL substrates, assuming a fixed Fermi level. c) Schematic conduction band diagram of perovskite film and different ETL substrates.

the methods reported by Edman and co-workers,[62–64] we exposed an as-prepared PCBM layer to UV light for some time, before DMF or perovskite solution casting. UV light creates a robust and less-soluble dimeric state of PCBM, yet with retained electronic properties. According to the XPS depth profiles, when using 10 mg mL^{-1} PCBM and UV light (**Figure 7**a,b), both DMF rinsed SnO_2/PCBM-dimer layers (w/wo thermal annealing) exhibit much higher carbon concentrations at the surface (>70 at%) than the SnO_2/PCBM reference (Figure 5a,b) due to a thicker PCBM layer on the SnO_2. This observation is well supported by the UV–vis–NIR measurement (Figure S13, Supporting Information) and the thickness of the capping PCBM layer (12 nm), measured by surface profilometry. Using a higher (20 mg mL^{-1}) PCBM concentration in combination with UV illumination, the depth profiles of both SnO_2/PCBM-dimer layers (w/wo thermal annealing) are similar to that of the SnO_2/C_{60} (35 nm) layer (Figure S12, Supporting Information) and show a constant carbon concentration of 100 at% during entire the sputtering process. Independent of w/wo thermal annealing, the PCBM thickness was 23 nm. This indicates the successful fabrication of a DMF-resilient SnO_2/PCBM bilayered ETL in which the thickness and the chemical interaction of the capping PCBM layer can be tuned, by modifying the PCBM solution concentration and the thermal annealing treatment. Figure 7a,b does not show a clear peak for the Sn and also the onset of the Si signal is much less clear than in Figure 5 for PCBM layers that were treated without UV light. We think that this is due to the fact that after UV illumination the rate of removal of the thin (12 nm) PCBM is drastically reduced and the Sn and Si signals results from regions below the top PCBM layer. This explanation is consistent with Figure 7c,d, where the thicker (23 nm) UV-treated PCBM layer is not removed and prevents observing Sn and Si below.

Figure 8 shows the *J–V* curves of PSC devices prepared with different concentrations of PCBM (5–20 mg mL^{-1}). Without exposure to UV light, all devices deliver virtually identical PCEs of 16.0% with negligible hysteresis when the PCBM layer is thermally annealed (Figure 8a and Table S6, Supporting Information). For low PCBM concentrations (≤10 mg mL^{-1}) only the PCBM chemically bonded to the SnO_2 is preserved at the interface. For the highest PCBM concentration (20 mg mL^{-1}) DMF rinsing does not wash away the entire PCBM layer but leaves an ≈13 nm film as determined by profilometry and confirmed by XPS depth profiling (Figure S14, Supporting Information). The results suggest that the passivation capacity of PCBM at the SnO_2 interface is largely independent of the concentrations of the PCBM solution and that, next to a surface bound monolayer, a thin (≈13 nm) residual PCBM layer offers no additional improvement.

© 2019 The Authors. Published by WILEY-VCH Verlag GmbH & Co. KGaA, Weinheim

16163028, 2019, 46, Downloaded from https://advanced.onlinelibrary.wiley.com/doi/10.1002/adfm.201905883 by Junke Wang - Oxford University , Wiley Online Library on [28/03/2026]. See the Terms and Conditions (https://onlinelibrary.wiley.com/terms-and-conditions) on Wiley Online Library for rules of use; OA articles are governed by the applicable Creative Commons License

16163028, 2019, 46, Downloaded from https://advanced.onlinelibrary.wiley.com/doi/10.1002/adfm.201905883 by Junke Wang - Oxford University , Wiley Online Library on [28/03/2026]. See the Terms and Conditions (https://onlinelibrary.wiley.com/terms-and-conditions) on Wiley Online Library for rules of use; OA articles are governed by the applicable Creative Commons License

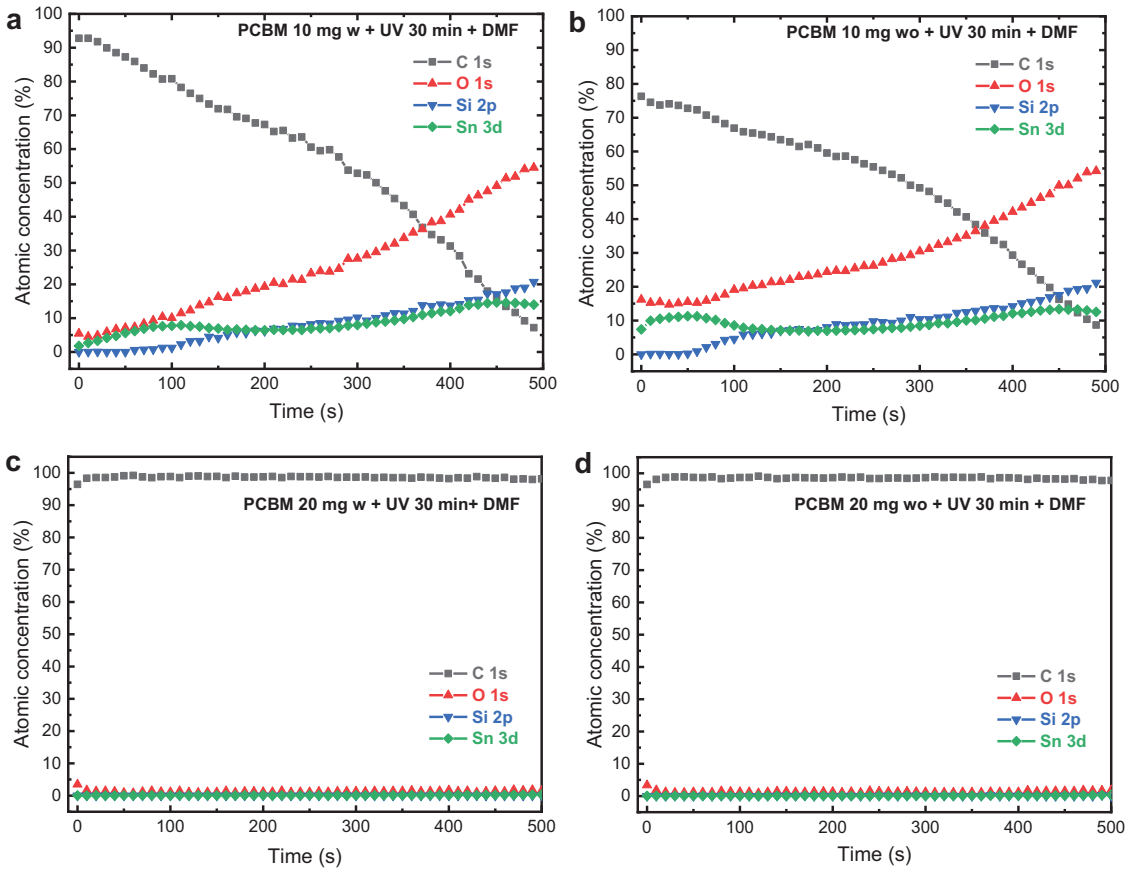

Figure 7. XPS depth profiles of glass/SnO_2 substrates passivated by 10 mg mL^{-1} PCBM a,b) with (w) or without (wo) thermal annealing and 20 mg mL^{-1} PCBM c–d) w/wo thermal annealing, respectively. All the samples were illuminated under UV light for 30 min in the N_2 atmosphere, before washing by DMF solvent. The initial SnO_2 layer thickness was ≈20 nm for all depth profiles.

In contrast, when using UV illumination to create PCBM dimers at the SnO_2 surface, a strong dependence of the PCE on the PCBM concentration is found, both with and without thermal annealing (Figure S15 and Tables S7 and S8, Supporting Information). At low PCBM concentrations (e.g., 10 mg mL^{-1}), thermally annealed PCBM-dimer layers provide high PCEs of ≈16.4%, comparable to devices without UV exposure, indicating that a thin PCBM-dimer layer gives good passivation (Figure 8b). Strikingly, the devices with not-annealed PCBM-dimer layer exhibit much inferior performance (PCE ≈ 14%; Figure 8b) despite the good coverage of the fullerene on the SnO_2 substrate (Figure 7b). We conclude that

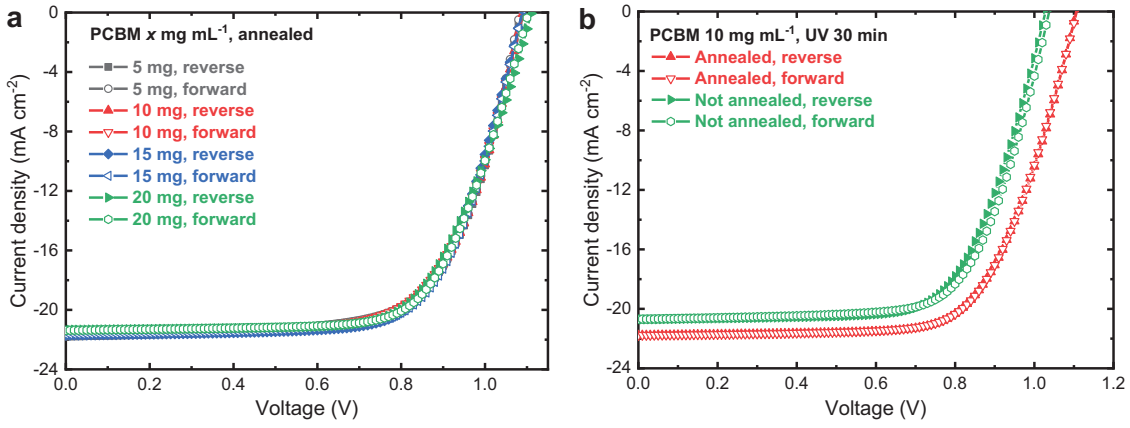

Figure 8. *J–V* curves of ITO/SnO_2/fullerene/$FA_{0.66}MA_{0.34}PbI_{2.85}Br_{0.15}$/Spiro-OMeTAD/$MoO_3$/Au solar cells with SnO_2/PCBM ETLs. a) For cells where the PCBM concentration in the spin coating solution varied from 5 to 20 mg mL^{-1} and the layers was thermally annealed (100 °C, 20 min). b) For cells made from a 10 mg mL^{-1} PCBM solution with or without thermal annealing and with UV-light illumination before the perovskite deposition.

© 2019 The Authors. Published by WILEY-VCH Verlag GmbH & Co. KGaA, Weinheim

16163028, 2019, 46, Downloaded from https://advanced.onlinelibrary.wiley.com/doi/10.1002/adfm.201905883 by Junke Wang - Oxford University , Wiley Online Library on [28/03/2026]. See the Terms and Conditions (https://onlinelibrary.wiley.com/terms-and-conditions) on Wiley Online Library for rules of use; OA articles are governed by the applicable Creative Commons License

the thermally induced chemical interaction between the PCBM and SnO_2 is the most influential factor in enhancing the interfacial charge transport process.

As the concentration of PCBM solution increases to 20 mg mL^{-1}, for both cells made with or without thermal annealing, the corresponding *J–V* curves show strong s-shapes with reduced V_{oc}, J_{sc}, and FF, yielding PCEs lower than 10% (Figure S15 and Tables S7 and S8, Supporting Information). Again, we exclude an effect of perovskite bulk films on the device performance, since they present virtually identical XRD patterns and SEM images on different PCBM-dimer layers (Figures S16 and S17, Supporting Information). In conductivity measurements for different ETLs (Figure S18 and Table S9, Supporting Information), we found that compared to other thin PCBM layers, the conductivity extracted from the *J–V* curve is reduced when applying a slightly thicker (20 mg mL^{-1}) PCBM-dimer layer on the SnO_2 substrate. This increased resistivity of the PCBM-dimer layer limits the charge transport and induces nonradiative recombination at the SnO_2/perovskite interface, resulting in the reduced device performance. Collectively, our observations imply that the fabrication of a robust SnO_2/fullerene ETL does not necessarily improve the SnO_2 passivation and that the introduction of a fullerene monolayer with controlled chemical interaction with the SnO_2 ETL is sufficient to boost the PSC device performance.

3. Conclusion

We performed a comprehensive study correlating the chemical interactions at the SnO_2/fullerene interface with the PSC device performance. XPS depth profile measurements are a useful tool to monitor the precise location of thin-film fullerene residues in the SnO_2 ETL. In the case of depositing PCBM from ≤10 mg mL^{-1} solutions, thermal annealing is essential to create a surface-bound PCBM monolayer that is resilient to depositing a perovskite layer on top. The surface-bound PCBM monolayer significantly improved the device performance and reproducibility. Although PCBM partly infiltrates into the porous SnO_2 layer, only the fullerenes located at the SnO_2/perovskite interface are essential for electron extraction. The passivation capacity of PCBM is not affected by the concentration of the solution from which it is deposited because PCBM that is not bound to the surface is removed by DMF in subsequent processing. While thermally evaporated C_{60} showed high resilience against DMF, the performance of the corresponding PSC was inferior to the thermally annealed PCBM devices. This is attributed to the absence of a chemical bond between C_{60} and the SnO_2 surface. In accordance, the carboxylic acid-based PCBA derivative exhibited much higher passivation efficiency. A PCBA monolayer with excellent coverage and DMF-resilience could be formed from dilute (0.2 mg mL^{-1}) solutions without any thermal treatment. After optimization, the best-performing device using a PCBA-modified SnO_2 ETL exhibited a PCE of 18.8%.

Interfaces are of significant importance for the PSCs based on metal-oxide layers. Depending on the fabrication method, the passivation of metal oxide is often found critical for high-performing devices. Our study explored the essence of the passivation layer between the photoactive and charge transport layers. The new insights into the interface passivation of metal oxide charge transport layer offers a strategy for the future development toward high-efficiency PSCs.

Supporting Information

Supporting Information is available from the Wiley Online Library or from the author.

Acknowledgements

The authors thank Dr. Mengmeng Li for the help with the AFM measurement. The authors acknowledge funding from the European Research Council under the European Union's Seventh Framework Programme (FP/2007-2013) (ERC Grant Agreement No. 339031), the Netherlands Organization for Scientific Research (NWO) (project 680-91-011), the Ministry of Education, Culture and Science (Gravity program 024.001.035), and the NWO Spinoza prize awarded to R.A.J. Janssen by the Netherlands Organization for Scientific Research (NWO).

Conflict of Interest

The authors declare no conflict of interest.

Keywords

fullerene, metal halide perovskite, passivation, solar cell, tin oxide

Received: July 20, 2019
Revised: August 21, 2019
Published online: September 16, 2019

[1] NREL Chart, https://www.nrel.gov/pv/assets/pdfs/best-research-cell-efficiencies-190416.pdf (accessed: June 2019).
[2] M. Saliba, J.-P. Correa-Baena, C. M. Wolff, M. Stolterfoht, N. Phung, S. Albrecht, D. Neher, A. Abate, *Chem. Mater.* **2018**, *30*, 4193.
[3] M. Saliba, T. Matsui, J. Y. Seo, K. Domanski, J. P. Correa-Baena, M. K. Nazeeruddin, S. M. Zakeeruddin, W. Tress, A. Abate, A. Hagfeldt, M. Gratzel, *Energy Environ. Sci.* **2016**, *9*, 1989.
[4] M. Saliba, T. Matsui, K. Domanski, J. Seo, A. Ummadisingu, S. M. Zakeeruddin, J. P. Correa Baena, W. R. Tress, A. Abate, A. Hagfeldt, M. Graetzel, *Science* **2016**, *354*, 206.
[5] W. S. Yang, B. W. Park, E. H. Jung, N. J. Joen, Y. C. Kim, D. U. Lee, S. S. Shin, J. Seo, E. K. Kim, J. H. Noh, S. I. Seok, *Science* **2017**, *356*, 1376.
[6] D. Luo, W. Yang, Z. Wang, A. Sadhanala, Q. Hu, R. Su, R. Shivanna, G. F. Trindade, J. F. Watts, Z. Xu, T. Liu, K. Chen, F. Ye, P. Wu, L. Zhao, J. Wu, Y. Tu, Y. Zhang, X. Yang, W. Zhang, R. H. Friend, Q. Gong, H. J. Snaith, R. Zhu, *Science* **2018**, *360*, 1442.
[7] Q. Jiang, Z. Chu, P. Wang, X. Yang, H. Liu, Y. Wang, Z. Yin, J. Wu, X. Zhang, J. You, *Adv. Mater.* **2017**, *29*, 1703852.
[8] H. Tan, A. Jain, O. Voznyy, X. Lan, F. P. G. De Arquer, J. Z. Fan, R. Quintero-Bermudez, M. Yuan, B. Zhang, Y. Zhao, F. Fan, P. Li, L. N. Quan, S. Hoogland, E. H. Sargent, *Science* **2017**, *355*, 722.
[9] Y. Galagan, *J. Phys. Chem. Lett.* **2018**, *9*, 4326.
[10] J. Wang, F. Di Giacomo, J. Brüls, H. Gorter, I. Katsouras, P. Groen, R. A. J. Janssen, R. Andriessen, Y. Galagan, *Sol. RRL* **2017**, *1*, 1700091.

© 2019 The Authors. Published by WILEY-VCH Verlag GmbH & Co. KGaA, Weinheim

[11] S. T. Williams, A. Rajagopal, C. C. Chueh, A. K. Jen, *J. Phys. Chem. Lett.* **2016**, *7*, 811.
[12] Y. Rong, Y. Hu, A. Mei, H. Tan, M. I. Saidaminov, S. I. Seok, M. D. McGehee, E. H. Sargent, H. Han, *Science* **2018**, *361*, eaat8235.
[13] H. Kim, K.-G. Lim, T.-W. Lee, *Energy Environ. Sci.* **2016**, *9*, 12.
[14] M. Liu, M. B. Johnston, H. J. Snaith, *Nature* **2013**, *501*, 395.
[15] S. D. Stranks, G. E. Eperon, G. Grancini, C. Menelaou, M. J. P. Alcocer, T. Leijtens, L. M. Herz, A. Petrozza, H. J. Snaith, *Science* **2013**, *342*, 341.
[16] M. A. Green, A. Ho-Baillie, H. J. Snaith, *Nat. Photonics* **2014**, *8*, 506.
[17] G. Xing, N. Mathews, S. Sun, S. S. Lim, Y. M. Lam, M. Graetzel, S. Mhaisalkar, T. C. Sum, *Science* **2013**, *342*, 344.
[18] M. A. Haque, A. D. Sheikh, X. Guan, T. Wu, *Adv. Energy Mater.* **2017**, *7*, 1602803.
[19] A. Mingorance, H. Xie, H.-S. Kim, Z. Wang, M. Balsells, A. Morales-Melgares, N. Domingo, N. Kazuteru, W. Tress, J. Fraxedas, N. Vlachopoulos, A. Hagfeldt, M. Lira-Cantu, *Adv. Mater. Interfaces* **2018**, *5*, 1800367.
[20] L. Xiong, Y. Guo, J. Wen, H. Liu, G. Yang, P. Qin, G. Fang, *Adv. Funct. Mater.* **2018**, *28*, 1802757.
[21] W. Ke, G. Fang, Q. Liu, L. Xiong, P. Qin, H. Tao, J. Wang, H. Lei, B. Li, J. Wan, G. Yang, Y. Yan, *J. Am. Chem. Soc.* **2015**, *137*, 6730.
[22] Q. Jiang, X. Zhang, J. You, *Small* **2018**, *14*, 1801154.
[23] Q. Jiang, L. Zhang, H. Wang, X. Yang, J. Meng, H. Liu, Z. Yin, J. Wu, X. Zhang, J. You, *Nat. Energy* **2017**, *2*, 16177.
[24] Y. Lee, S. Lee, G. Seo, S. Paek, K. T. Cho, A. J. Huckaba, M. Calizzi, D. W. Choi, J. S. Park, D. Lee, H. J. Lee, A. M. Asiri, M. K. Nazeeruddin, *Adv. Sci.* **2018**, *5*, 1800130.
[25] J. P. Correa Baena, L. Steier, W. Tress, M. Saliba, S. Neutzner, T. Matsui, F. Giordano, T. J. Jacobsson, A. R. Srimath Kandada, S. M. Zakeeruddin, A. Petrozza, A. Abate, M. K. Nazeeruddin, M. Grätzel, A. Hagfeldt, *Energy Environ. Sci.* **2015**, *8*, 2928.
[26] M. F. Ayguler, A. G. Hufnagel, P. Rieder, M. Wussler, W. Jaegermann, T. Bein, V. Dyakonov, M. L. Petrus, A. Baumann, P. Docampo, *ACS Appl. Mater. Interfaces* **2018**, *10*, 11414.
[27] Y. Kuang, V. Zardetto, R. van Gils, S. Karwal, D. Koushik, M. A. Verheijen, L. E. Black, C. Weijtens, S. Veenstra, R. Andriessen, W. M. M. Kessels, M. Creatore, *ACS Appl. Mater. Interfaces* **2018**, *10*, 30367.
[28] E. H. Anaraki, A. Kermanpur, L. Steier, K. Domanski, T. Matsui, W. Tress, M. Saliba, A. Abate, M. Grätzel, A. Hagfeldt, J.-P. Correa-Baena, *Energy Environ. Sci.* **2016**, *9*, 3128.
[29] Q. Jiang, Y. Zhao, X. Zhang, X. Yang, Y. Chen, Z. Chu, Q. Ye, X. Li, Z. Yin, J. You, *Nat. Photonics* **2019**, *13*, 460.
[30] K. Choi, J. Lee, H. I. Kim, C. W. Park, G.-W. Kim, H. Choi, S. Park, S. A. Park, T. Park, *Energy Environ. Sci.* **2018**, *11*, 3238.
[31] S. A. L. Weber, I. M. Hermes, S.-H. Turren-Cruz, C. Gort, V. W. Bergmann, L. Gilson, A. Hagfeldt, M. Graetzel, W. Tress, R. Berger, *Energy Environ. Sci.* **2018**, *11*, 2404.
[32] I. M. Hermes, Y. Hou, V. W. Bergmann, C. J. Brabec, S. A. L. Weber, *J. Phys. Chem. Lett.* **2018**, *9*, 6249.
[33] L. Zuo, Q. Chen, N. De Marco, Y. T. Hsieh, H. Chen, P. Sun, S. Y. Chang, H. Zhao, S. Dong, Y. Yang, *Nano Lett.* **2017**, *17*, 269.
[34] M. Stolterfoht, C. M. Wolff, J. A. Márquez, S. Zhang, C. J. Hages, D. Rothhardt, S. Albrecht, P. L. Burn, P. Meredith, T. Unold, D. Neher, *Nat. Energy* **2018**, *3*, 847.
[35] K. Liu, S. Chen, J. Wu, H. Zhang, M. Qin, X. Lu, Y. Tu, Q. Meng, X. Zhan, *Energy Environ. Sci.* **2018**, *11*, 3463.
[36] T. Gatti, E. Menna, M. Meneghetti, M. Maggini, A. Petrozza, F. Lamberti, *Nano Energy* **2017**, *41*, 84.
[37] W. Ke, D. Zhao, C. Xiao, C. Wang, A. J. Cimaroli, C. R. Grice, M. Yang, Z. Li, C.-S. Jiang, M. Al-Jassim, K. Zhu, M. G. Kanatzidis, G. Fang, Y. Yan, *J. Mater. Chem. A* **2016**, *4*, 14276.
[38] L. Kegelmann, C. M. Wolff, C. Awino, F. Lang, E. L. Unger, L. Korte, T. Dittrich, D. Neher, B. Rech, S. Albrecht, *ACS Appl. Mater. Interfaces* **2017**, *9*, 17245.
[39] D. Yang, R. Yang, K. Wang, C. Wu, X. Zhu, J. Feng, X. Ren, G. Fang, S. Priya, S. F. Liu, *Nat. Commun.* **2018**, *9*, 3239.
[40] S. P. Pujari, L. Scheres, A. T. Marcelis, H. Zuilhof, *Angew. Chem., Int. Ed.* **2014**, *53*, 6322.
[41] W.-Q. Wu, D. Chen, R. A. Caruso, Y.-B. Cheng, *J. Mater. Chem. A* **2017**, *5*, 10092.
[42] Z. Tebby, T. Uddin, Y. Nicolas, C. Olivier, T. Toupance, C. Labrugere, L. Hirsch, *ACS Appl. Mater. Interfaces* **2011**, *3*, 1485.
[43] K. Wojciechowski, S. D. Stranks, A. Abate, G. Sadoughi, A. Sadhanala, N. Kopidakis, G. Rumbles, C.-Z. Li, R. H. Friend, A. K.-Y. Jen, H. J. Snaith, *ACS Nano* **2014**, *8*, 12701.
[44] C. Wang, D. Zhao, C. R. Grice, W. Liao, Y. Yu, A. Cimaroli, N. Shrestha, P. J. Roland, J. Chen, Z. Yu, P. Liu, N. Cheng, R. J. Ellingson, X. Zhao, Y. Yan, *J. Mater. Chem. A* **2016**, *4*, 12080.
[45] C. Wang, D. Zhao, Y. Yu, N. Shrestha, C. R. Grice, W. Liao, A. J. Cimaroli, J. Chen, R. J. Ellingson, X. Zhao, Y. Yan, *Nano Energy* **2017**, *35*, 223.
[46] C. Wang, C. Xiao, Y. Yu, D. Zhao, R. A. Awni, C. R. Grice, K. Ghimire, I. Constantinou, W. Liao, A. J. Cimaroli, P. Liu, J. Chen, N. J. Podraza, C.-S. Jiang, M. M. Al-Jassim, X. Zhao, Y. Yan, *Adv. Energy Mater.* **2017**, *7*, 1700414.
[47] Y. Dong, W. Li, X. Zhang, Q. Xu, Q. Liu, C. Li, Z. Bo, *Small* **2016**, *12*, 1098.
[48] K. K. Wong, A. Fakharuddin, P. Ehrenreich, T. Deckert, M. Abdi-Jalebi, R. H. Friend, L. Schmidt-Mende, *J. Phys. Chem. C* **2018**, *122*, 10691.
[49] Q. An, P. Fassl, Y. J. Hofstetter, D. Becker-Koch, A. Bausch, P. E. Hopkinson, Y. Vaynzof, *Nano Energy* **2017**, *39*, 400.
[50] Y. Zhang, P. Wang, X. Yu, J. Xie, X. Sun, H. Wang, J. Huang, L. Xu, C. Cui, M. Lei, D. Yang, *J. Mater. Chem. A* **2016**, *4*, 18509.
[51] K. Wojciechowski, T. Leijtens, S. Siprova, C. Schlueter, M. T. Horantner, J. T. Wang, C. Z. Li, A. K.-Y. Jen, T. L. Lee, H. J. Snaith, *J. Phys. Chem. Lett.* **2015**, *6*, 2399.
[52] C. Tao, S. Neutzner, L. Colella, S. Marras, A. R. Srimath Kandada, M. Gandini, M. D. Bastiani, G. Pace, L. Manna, M. Caironi, C. Bertarelli, A. Petrozza, *Energy Environ. Sci.* **2015**, *8*, 2365.
[53] C. Tao, J. Van Der Velden, L. Cabau, N. F. Montcada, S. Neutzner, A. R. Srimath Kandada, S. Marras, L. Brambilla, M. Tommasini, W. Xu, R. Sorrentino, A. Perinot, M. Caironi, C. Bertarelli, E. Palomares, A. Petrozza, *Adv. Mater.* **2017**, *29*, 1604493.
[54] B. L. Watson, N. Rolston, K. A. Bush, T. Leijtens, M. D. McGehee, R. H. Dauskardt, *ACS Appl. Mater. Interfaces* **2016**, *8*, 25896.
[55] W. Qiu, J. P. Bastos, S. Dasgupta, T. Merckx, I. Cardinaletti, M. V. C. Jenart, C. B. Nielsen, R. Gehlhaar, J. Poortmans, P. Heremans, I. McCulloch, D. Cheyns, *J. Mater. Chem. A* **2017**, *5*, 2466.
[56] X. Liu, Y. Zhang, L. Shi, Z. Liu, J. Huang, J. S. Yun, Y. Zeng, A. Pu, K. Sun, Z. Hameiri, J. A. Stride, J. Seidel, M. A. Green, X. Hao, *Adv. Energy Mater.* **2018**, *8*, 1800138.
[57] T. Bu, J. Li, F. Zheng, W. Chen, X. Wen, Z. Ku, Y. Peng, J. Zhong, Y. B. Cheng, F. Huang, *Nat. Commun.* **2018**, *9*, 4609.
[58] B. Tu, Y. Shao, W. Chen, Y. Wu, X. Li, Y. He, J. Li, F. Liu, Z. Zhang, Y. Lin, X. Lan, L. Xu, X. Shi, A. M. C. Ng, H. Li, L. W. Chung, A. B. Djurisic, Z. He, *Adv. Mater.* **2019**, *31*, 1805944.
[59] H. Yoon, S. M. Kang, J.-K. Lee, M. Choi, *Energy Environ. Sci.* **2016**, *9*, 2262.
[60] K. Wojciechowski, I. Ramirez, T. Gorisse, O. Dautel, R. Dasari, N. Sakai, J. M. Hardigree, S. Song, S. Marder, M. Riede, G. Wantz, H. J. Snaith, *ACS Energy Lett.* **2016**, *1*, 648.
[61] S. Song, R. Hill, K. Choi, K. Wojciechowski, S. Barlow, J. Leisen, H. J. Snaith, S. R. Marder, T. Park, *Nano Energy* **2018**, *49*, 324.

© 2019 The Authors. Published by WILEY-VCH Verlag GmbH & Co. KGaA, Weinheim

16163028, 2019, 46, Downloaded from https://advanced.onlinelibrary.wiley.com/doi/10.1002/adfm.201905883 by Junke Wang - Oxford University , Wiley Online Library on [28/03/2026]. See the Terms and Conditions (https://onlinelibrary.wiley.com/terms-and-conditions) on Wiley Online Library for rules of use; OA articles are governed by the applicable Creative Commons License

[62] J. Wang, C. Larsen, T. Wågberg, L. Edman, *Adv. Funct. Mater.* **2011**, *21*, 3723.
[63] J. Enevold, C. Larsen, J. Zakrisson, M. Andersson, L. Edman, *Nano Lett.* **2018**, *18*, 540.
[64] A. Dzwilewski, T. Wågberg, L. Edman, *J. Am. Chem. Soc.* **2009**, *131*, 4006.
[65] W. Qiu, A. Ray, M. Jaysankar, T. Merckx, J. P. Bastos, D. Cheyns, R. Gehlhaar, J. Poortmans, P. Heremans, *Adv. Funct. Mater.* **2017**, *27*, 1700920.
[66] O. Pachoumi, A. A. Bakulin, A. Sadhanala, H. Sirringhaus, R. H. Friend, Y. Vaynzof, *J. Phys. Chem. C* **2014**, *118*, 18945.
[67] K. H. Hendriks, J. J. van Franeker, B. J. Bruijnaers, J. A. Anta, M. M. Wienk, R. A. J. Janssen, *J. Mater. Chem. A* **2017**, *5*, 2346.
[68] W. S. Yang, J. H. Noh, N. J. Joen, Y. C. Kim, S. Ryu, J. Seo, S. I. Seok, *Science* **2015**, *348*, 1234.
[69] J. Tian, Q. Xue, X. Tang, Y. Chen, N. Li, Z. Hu, T. Shi, X. Wang, F. Huang, C. J. Brabec, H. L. Yip, Y. Cao, *Adv. Mater.* **2019**, *31*, 1901152.
[70] S. Zhang, M. Stolterfoht, A. Armin, Q. Lin, F. Zu, J. Sobus, H. Jin, N. Koch, P. Meredith, P. L. Burn, D. Neher, *ACS Appl. Mater. Interfaces* **2018**, *10*, 21681.
[71] Y. Vaynzof, D. Kabra, L. Zhao, P. K. H. Ho, A. T. S. Wee, R. H. Friend, *Appl. Phys. Lett.* **2010**, *97*, 033309.

© 2019 The Authors. Published by WILEY-VCH Verlag GmbH & Co. KGaA, Weinheim

16163028, 2019, 46, Downloaded from https://advanced.onlinelibrary.wiley.com/doi/10.1002/adfm.201905883 by Junke Wang - Oxford University , Wiley Online Library on [28/03/2026]. See the Terms and Conditions (https://onlinelibrary.wiley.com/terms-and-conditions) on Wiley Online Library for rules of use; OA articles are governed by the applicable Creative Commons License